Microwave Encephalography (MWEG) Reveals a Novel Electromagnetic Correlate of Higher Nervous Activity

Leonid I. Brusilovsky[1], Andrey S. Bryukhovetskiy[2]

[1] ELBRUS Corporation LLC, Moscow, Russia
[2] FSBI National Medical Research Center for Obstetrics, Gynecology and Perinatology named after Academician V.I. Kulakov, Moscow, Russia

Corresponding author: Leonid I. Brusilovsky, netsrv@aha.ru, ORCID: 0000-0002-8291-5532

Abstract

The search for physical correlates of higher nervous activity remains a fundamental challenge in neuroscience. Here we report the discovery of a previously unknown electromagnetic phenomenon – the brain's own ultra-weak microwave emissions in the 1–5 GHz range, detected non-invasively using a novel method called microwave encephalography (MWEG). Through systematic experiments spanning 2016–2025, we demonstrate that these signals are endogenous, arising from neural activity rather than thermal noise or external interference. Using a simple light/darkness visual paradigm, we found a robust functional hemispheric asymmetry: the right occipital region exhibited significantly higher emission in darkness ($p < 0.001$), whereas the left occipital region was more active in light ($p < 0.001$). This pattern was replicated in a group study (three subjects, $p < 0.05$ for right, $p < 0.01$ for left). The signals represent a modulation of the thermal background by cognitive state, providing a new physical dimension of brain function. Two complementary mathematical models are proposed – an energy-based model linking optical input to microwave emission, and an information-based model interpreting spectral changes as structural pattern overlap with memory engrams. These findings open a new avenue for non-invasive study of cognitive processes and may have future applications in neurodiagnostics.

Keywords: microwave encephalography, higher nervous activity, functional hemispheric asymmetry, cognitive states, non-invasive brain monitoring, electromagnetic correlates of consciousness

1. Introduction

Understanding how the brain generates cognition and consciousness remains one of the greatest challenges in neuroscience. Despite decades of research using electroencephalography (EEG), magnetoencephalography (MEG), and functional magnetic resonance imaging (fMRI), fundamental limitations persist. EEG provides high temporal resolution but low spatial resolution and requires galvanic contact [1]; MEG offers excellent spatiotemporal resolution but demands expensive shielding and cryogenic equipment [2]; fMRI measures slow hemodynamic responses and requires immobilization [3]. None of these methods allow continuous, non-invasive monitoring of brain activity in natural conditions.

In 2014, Bryukhovetskiy proposed an information-commutation theory of the human brain, suggesting that cognitive processes involve electromagnetic interactions within the cerebrospinal fluid (CSF) system and the meninges [4,5]. According to this hypothesis, CSF spaces may act as dynamic resonators or waveguides, generating ultra-weak microwave emissions that carry information about brain activity. This idea stimulated the search for new physical methods to detect such emissions.

Here we report the discovery of a previously unknown electromagnetic correlate of higher nervous activity – the brain's own microwave radiation in the 1–5 GHz range, which we term microwave encephalography (MWEG). Using high-end spectrum analyzers in shielded anechoic chambers, we detected signals with power levels of –130 to –100 dBm (10^{-16}–10^{-13} W) [6,7]. Through nine years of systematic experimentation, we have:

1. Demonstrated the endogenous origin of these signals.
2. Discovered a robust functional hemispheric asymmetry during visual stimulation.
3. Shown that these signals are modulated by cognitive state (light/darkness).
4. Developed two complementary mathematical models linking optical input to microwave emission.

These findings reveal a new physical dimension of brain function and provide a potential non-invasive tool for studying cognitive states.

2. Materials and Methods

2.1. Experimental setup

All experiments were conducted in anechoic shielded chambers (attenuation ≥100 dB in the 1–40 GHz range) at accredited test laboratories (FBU "Rostest-Moscow", FSUE TsENKI, and FBU "Nizhny Novgorod CSM"). The primary instrument was a Rohde & Schwarz FSW series spectrum analyzer (models FSW26, FSW43, ESW44) operating in FFT mode. Settings: span 4 GHz (1–5 GHz), resolution bandwidth 300 Hz for scanning, 4001 sweep points, video bandwidth 200 Hz, preamplifier on. Log-periodic antennas R&S HL050 and P6-222M were used with built-in or external low-noise amplifiers. A typical setup is shown in Figure 1.

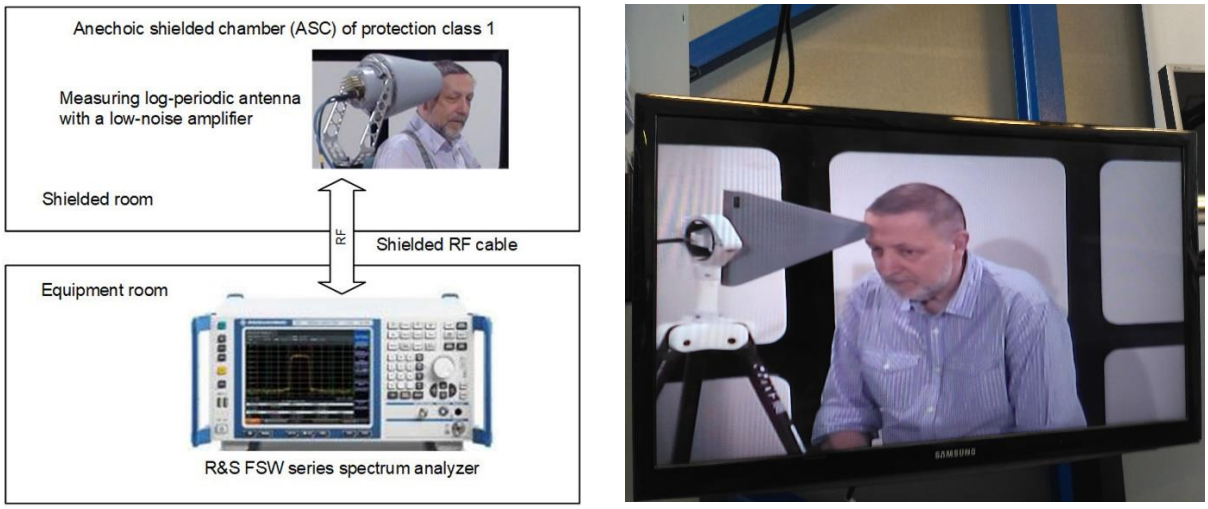

Fig. 1. Typical experimental setup in an anechoic shielded chamber: (a) schematic; (b) photograph from the 2021 experiment.

2.2. Participants and protocols

Early experiments (2016–2019). A two-step adaptive protocol (PMI_1) was used: fast scanning (300 Hz) to detect candidate "substantial spikes" (local peaks exceeding background by a threshold), followed by high-resolution scanning (30 Hz) for confirmation. Control measurements included background spectra, recordings from a saline phantom (37°C), and recordings from different body parts.

2021 experiment (July 12–13, 2021, FBU "Rostest-Moscow") – one healthy male subject (66 years). A total of 138 measurements were made over five series. Series 1, 2, 4, 5 recorded from the right occipital area (59 light–darkness pairs); series 3 from the left occipital area (10 pairs). Stimuli: light (1000 lx) and complete darkness (<0.01 lx), eyes open, 3 min per state. A single-step protocol (PMI_2) was used: scanning with 300 Hz and automated analysis of digitized amplitude-frequency characteristics (AFC) using custom Python software (MWENC, SSPIKES). The spike detection threshold was 2.2 dB.

2025 experiment (March 12, 2025, FBU "Nizhny Novgorod CSM") – three healthy male volunteers (age 45–70 years). Recordings from the right and left occipital areas (8 measurements per side per subject, total 96 measurements). Stimuli: light (1000 lx) and complete darkness, eyes open, 3 min per state. The same protocol and software were used. Data are openly available at Zenodo (DOI: 10.5281/zenodo.15739578).

All procedures were performed in accordance with the 2013 Helsinki Declaration; informed consent was obtained.

2.3. Data processing and statistics

The MWENC program counted "substantial spikes" – points where signal power exceeded the averaged background by the threshold (2.2 dB for 2021, 22 dB for 2025). For each measurement, the number of spikes was recorded.

For statistical analysis, the difference in spike counts between paired light and darkness conditions ($d = N_{\text{dark}} - N_{\text{light}}$) was used. A paired t-test (function scipy.stats.ttest_rel in Python 3.9) was applied; normality was verified by the Shapiro–Wilk test ($p > 0.05$). Significance was set at $p < 0.05$. To evaluate discriminative power, receiver operating characteristic (ROC) analysis was performed; the area under the curve (AUC) was computed for each hemisphere.

3. Results

3.1. Confirmation of endogenous origin (2016–2019)

The number of substantial spikes recorded from the head was 10–100 times higher than from background or phantom. Recordings from the hand, neck, and abdomen produced almost no spikes (Table 1). Changing antennas or amplifiers did not alter the pattern, confirming that the signals originate from the brain.

Table 1. Summary of control experiments (2016–2019)

Test condition	Typical number of spikes per sweep	Remarks
Background (empty chamber)	0–4	Stable, no systematic patterns
Phantom (saline, 37°C)	0–3	Random, no correlation with stimulus
Human head (occipital, temporal, parietal)	30–150	Rich structure, reproducible patterns
Human hand, neck, abdomen	0–5	Close to background

3.2. 2021 experiment

In the right hemisphere (series 1,2,4,5; 59 pairs), the mean difference (darkness–light) was +4.75 ($t(58) = 4.00$, $p < 0.001$). In the left hemisphere (series 3; 10 pairs), the mean difference was –28.1 ($t(9) = -8.20$, $p < 0.001$) (Table 2). Thus, the right hemisphere is significantly more active in darkness, the left in light. Representative amplitude-frequency characteristics and spike distributions are shown in Figures 2 and 3.

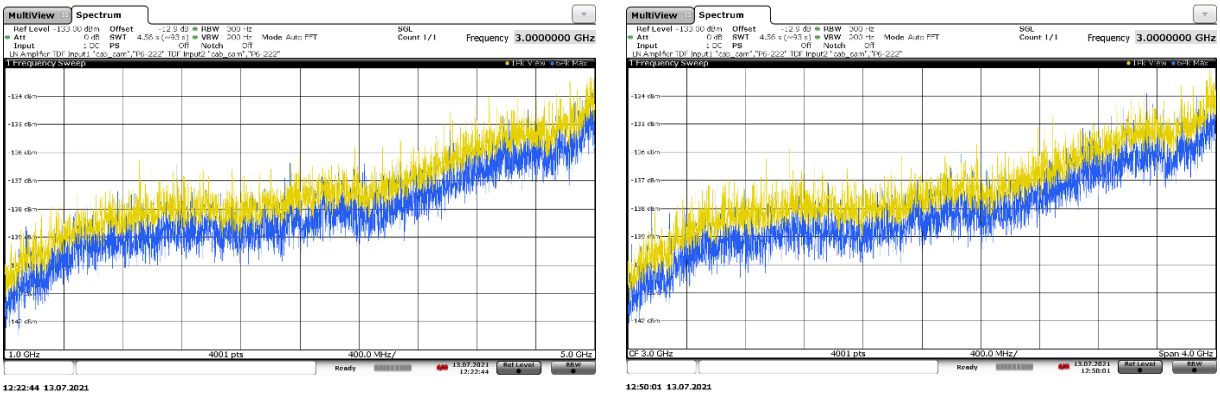

(a) (b)

Fig. 2. Example of amplitude-frequency characteristics (AFC) from the right occipital area (blue) and background (yellow) recorded in the 2021 experiment, series 2, experiment 4: (a) light stimulus; (b) darkness stimulus. Background is an average of 10 sweeps.

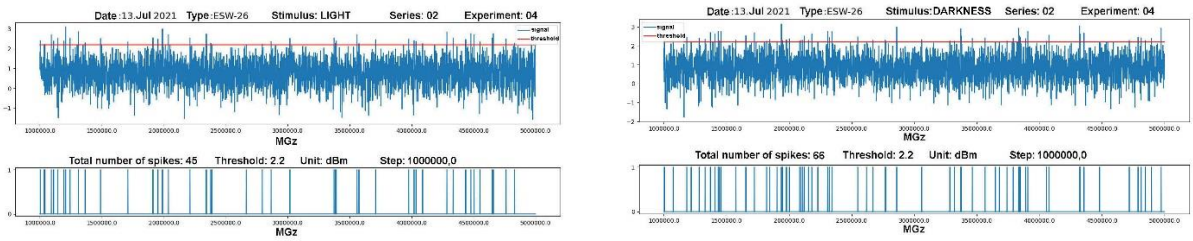

(a) (b)

Fig. 3. Spike extraction by the MWENC program for the same AFC as in Fig. 2. Upper panel: original AFC with detected spikes; lower panel: distribution of spikes along the frequency axis (microwave encephalogram). (a) light; (b) darkness.

Table 2. Results of the 2021 experiment (paired t-test)

Series	Side	n	Light (M ± SEM)	Darkness (M ± SEM)	Difference (d)	t-statistic	p (two-tailed)
1	Right	19	67.7 ± 1.5	72.9 ± 1.6	+5.26	2.53	0.020
2	Right	10	39.8 ± 2.0	53.0 ± 2.4	+13.2	4.04	0.003
3	Left	10	68.6 ± 1.8	40.5 ± 2.2	–28.1	–8.20	<0.001
4	Right	10	42.8 ± 1.5	45.7 ± 1.8	+2.90	1.26	0.241
5	Right	20	33.5 ± 0.7	34.5 ± 0.8	+0.85	0.57	0.577
1+2+4+5	Total right	59	47.2 ± 1.7	51.9 ± 1.9	+4.75	4.00	<0.001

3.3. 2025 group study

The results from three subjects confirmed the asymmetry (Table 3). For the right hemisphere, spikes were significantly higher in darkness ($p < 0.05$); for the left hemisphere, higher in light ($p < 0.01$). Figure 4 shows the mean spike counts with SEM.

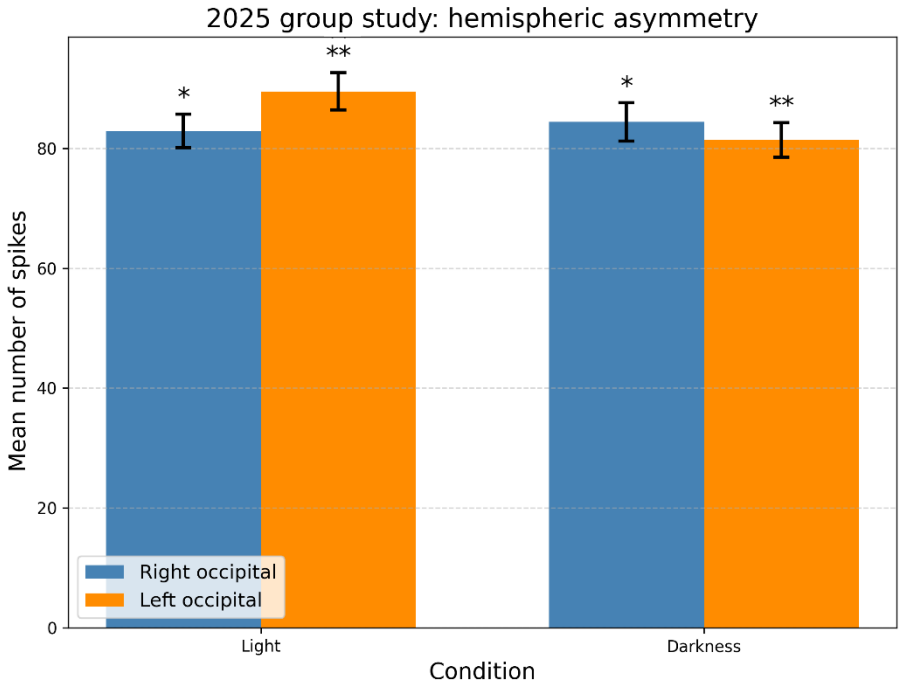

Fig. 4. Results of the 2025 group study: mean number of spikes (± SEM) for right and left occipital areas under light and darkness conditions. Blue bars: right hemisphere; red bars: left hemisphere. Asterisks: * $p < 0.05$, ** $p < 0.01$.

Table 3. Results of the 2025 experiment (M ± SEM, n = 8 per subject and side)

Region	Light	Darkness	Difference	t-statistic	p
Right occipital	82.9 ± 2.8	84.4 ± 3.2	+1.5	2.31	<0.05
Left occipital	89.5 ± 3.1	81.4 ± 2.9	–8.1	6.75	<0.01

3.4. ROC analysis

Using spike count as a classifier for light vs. darkness, AUC values were: right hemisphere 0.71 (95% CI: 0.64–0.78), left hemisphere 0.83 (95% CI: 0.76–0.90), indicating moderate to good discriminative power.

4. Discussion

4.1. A novel electromagnetic correlate of higher nervous activity

This study establishes that the human brain emits ultra-weak microwaves (1–5 GHz) that are modulated by cognitive state. The signals are endogenous, as shown by their absence from phantoms and non-neural body parts, and by their stability across different antennas and amplifiers. Importantly, the thermal radiation power of the head at 310 K is ~10^{-11} W/Hz [8], orders of magnitude higher than the recorded signal level (10^{-16}–10^{-13} W). Thus, the observed spikes represent not independent emission but a **modulation of the thermal background** caused by changes in the electrodynamic properties of neural tissue during cognitive activity.

4.2. Functional hemispheric asymmetry

The most striking finding is the clear lateralization of this modulation. The right hemisphere shows significantly higher activity in darkness, whereas the left hemisphere responds more strongly to light. This pattern aligns with established neurophysiological knowledge: the right hemisphere is dominant in vigilance, spatial attention, and the default mode network, which is activated in the absence of external tasks [9,10]. The left hemisphere specializes in analytical processing of sensory information [11]. Light stimulus thus engages left-hemisphere visual mechanisms, while darkness enhances endogenous right-hemisphere activity. Our quantitative data provide the first demonstration that this well-known asymmetry can be captured by passive microwave recording, offering a new window into cognitive states.

4.3. Possible physical mechanisms

The frequency range 1–5 GHz corresponds to wavelengths in brain tissue ($\varepsilon \approx 45$) of 45–9 mm, matching the scale of large neural ensembles (macrocolumns 3–10 mm), thalamic nuclei (5–10 mm), and CSF spaces (1–3 mm to several cm). This suggests that the observed spectral peaks may arise from eigenmodes in these structures [4,5]. The signals likely reflect collective, synchronized neural activity that modulates local dielectric properties and generates a detectable microwave signature. Two complementary mathematical models were developed to describe this process: an energy-based model linking optical input to microwave emission via neural mode dynamics, and an information-based model interpreting spectral changes as structural overlap with memory engrams (full derivations in Supplementary Materials).

4.4. Comparison with existing methods

MWEG offers several potential advantages over current neuroimaging techniques: (1) non-contact (no electrodes), (2) portability, (3) high temporal resolution, and (4) sensitivity to new physical quantities (ion dynamics, membrane polarization, CSF oscillations). Unlike fMRI, it does not require immobilization; unlike MEG, it does not need cryogenic shielding; unlike EEG, it is truly contactless. This makes it a promising tool for long-term monitoring in natural settings.

4.5. Limitations and future directions

Limitations include small sample sizes and the lack of simultaneous recordings with reference methods (EEG, fMRI). The origin of the signal – whether neuronal, glial, or CSF-mediated – remains to be fully

elucidated. Future work should focus on larger cohorts, multi-channel antenna arrays for spatial localization, and validation against established techniques.

5. Conclusions

1. Systematic experiments (2016–2025) have revealed a previously unknown electromagnetic correlate of higher nervous activity – the brain's own ultra-weak microwave emissions (1–5 GHz), which are endogenous and modulated by cognitive state.
2. A robust functional hemispheric asymmetry was identified: the right hemisphere is more active in darkness, the left in light ($p < 0.001$ in 2021, $p < 0.05$ and $p < 0.01$ in 2025). This pattern aligns with known hemispheric specialization and demonstrates that MWEG captures cognitively relevant information.
3. The signals represent a modulation of the thermal background by neural activity, providing a new physical dimension of brain function.
4. Two complementary mathematical models are proposed (detailed in Supplementary Materials), offering a framework for interpreting the observed spectral changes.
5. MWEG opens new perspectives for non-invasive, portable assessment of cognitive states and may have future applications in neurodiagnostics and cognitive monitoring.

Data Availability

All data from the 2025 experiment are openly available at Zenodo: https://doi.org/10.5281/zenodo.15739578.

Acknowledgments

The authors thank the staff of the test laboratories FBU "Rostest-Moscow", FSUE TsENKI, and FBU "Nizhny Novgorod CSM" for technical assistance, and RADIAN LLC, ATON LLC for equipment support.

Funding

This work was supported by ELBRUS Corporation LLC, ARKUS LLC, ALMAZ-SP JSC, VEK MC LLC, and Mr. A.A. Akimov. The sponsors had no role in study design, data collection, analysis, or manuscript preparation.

Conflict of Interest

The authors declare no competing financial interests.

Declaration of Generative AI Use

During the preparation of this work, AI-assisted tools were used solely to improve language and readability. After using these tools, the authors reviewed and edited the content as needed and take full responsibility for the final manuscript.

References

[1] Novikova E.Y., Ivanov A.A. Minimal standards for routine EEG examinations and sleep EEG IFCN & ILAE 2023: general review and assessment of applicability in Russia. Epilepsy and Paroxysmal Conditions. 2024;16(3):278–287. https://doi.org/10.17749/2077-8333/epi.par.con.2024.189

[2] Shestakova A.N., Butorina A.V., Osadchiy A.E., Shtyrov Y.Y. Magnetoencephalography – the newest method of functional brain mapping in humans. Experimental Psychology. 2012;5(2):119–134.

[3] Logothetis N.K., Pauls J., Augath M., Trinath T., Oeltermann A. Neurophysiological investigation of the basis of the fMRI signal. Nature. 2001;412:150–157. doi: 10.1038/35084005

[4] Bryukhovetskiy A.S. Problems of Theoretical Neurology: Information-Commutation Device and Principles of Human Brain Function. Moscow: Poligraf-Plus; 2014. (In Russian)

[5] Bryukhovetskiy A.S. Human Brain Theory. Information-Commutation Device of the Brain and Principles of its Work and Modeling. New York: Nova Science Publishers; 2016.

[6] Brusilovsky L.I., Bryukhovetskiy A.S., Kozhin S.P., et al. Experimental studies of microwave electromagnetic activity of the human brain. Journal of Radio Electronics. 2020;(2). doi: 10.18127/j15604128-202003-05 (In Russian)

[7] Bryukhovetskiy A.S., Brusilovsky L.I., Kozhin S.P., et al. Human mind has microwave electromagnetic nature and can be recorded and processed. Progress in Brain Research. 2020;258:439–462. doi: 10.1016/bs.pbr.2020.09.006

[8] Petrosyan V.I., Sinitsyn P.P., Elkin V.A., et al. The role of resonant molecular-wave processes in nature and their use for monitoring and correcting ecological systems. Biomedical Radioelectronics. 2001;(5–6):62–129. (In Russian)

[9] Corbetta M., Shulman G.L. Control of goal-directed and stimulus-driven attention in the brain. Nat Rev Neurosci. 2002;3(3):201–215. doi: 10.1038/nrn755

[10] Weintraub S., Mesulam M.M. Right cerebral dominance in spatial attention: further evidence based on ipsilateral neglect. Arch Neurol. 1987;44(6):621–625. doi: 10.1001/archneur.1987.00520180043014

[11] Aftanas L.I., Reva N.V., Pavlov S.V., et al. Linkage of Brain Oscillatory Systems with the Cognitive (experience and valence) and Physiological (cardiovascular reactivity) Components of the Emotions. Neuroscience and Behavioral Physiology. 2015;45(6):660-667. doi: 10.1007/s11055-015-0165-x

Supplementary Materials

The complete derivations of the mathematical models, additional experimental data, and extended methodological details are provided in the online Supplementary Materials.

Supplementary Materials

Microwave Encephalography (MWEG) Reveals a Novel Electromagnetic Correlate of Higher Nervous Activity

Leonid I. Brusilovsky, Andrey S. Bryukhovetskiy

S1. Complete Derivation of the Energy-Based Model

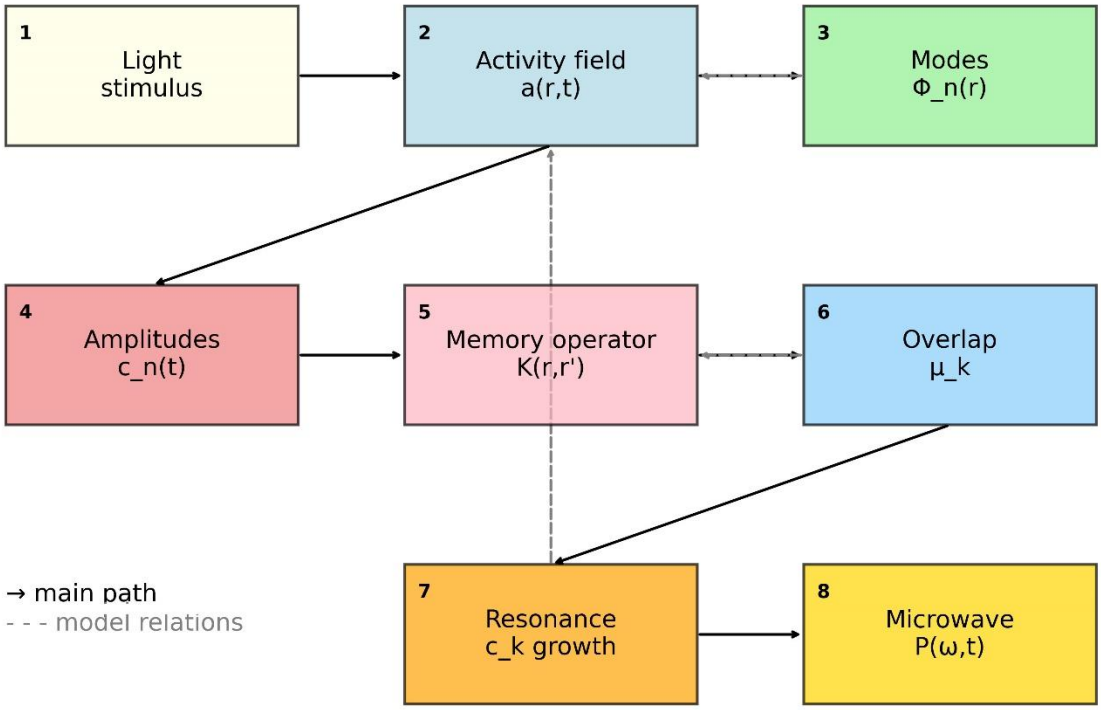

Fig S1. Schematic representation of the energy-based model of microwave generation.

The diagram illustrates the flow of physical quantities from the visual stimulus to the recorded microwave emission, presented in Section 4.3 of the main text.

- **Block 1 (Light stimulus):** External visual input (light on/off) that initiates the process.
- **Block 2 (Activity field a(r,t)):** Continuous neural activity field representing local field potentials or spike densities in the visual cortex.
- **Block 3 (Modes $\Phi_n(r)$):** Spatial eigenmodes obtained by decomposing the activity field; each mode corresponds to a stable excitation pattern (e.g., cortical columns, CSF resonances).
- **Block 4 (Amplitudes $c_n(t)$):** Complex amplitudes that quantify the contribution of each mode to the total activity; their dynamics are governed by Eq. (2).
- **Block 5 (Memory operator K(r,r')):** Integral operator representing long-term synaptic changes; its kernel is expanded over engrams Ψ_n with weights λ_n (Eq. (3)).
- **Block 6 (Overlap μ_k):** Projection of the current field onto the k-th engram (Eq. (4)); it measures how close the current pattern is to a stored memory.
- **Block 7 (Resonance c_k growth):** When spatial and frequency resonance conditions are satisfied, the corresponding amplitude grows nonlinearly (Eq. (5)), corresponding to memory retrieval.
- **Block 8 (Microwave P(ω,t)):** The emitted microwave power, proportional to the squared sum of the time derivatives of the amplitudes (Eq. (6)), serving as the observable signal.

Arrows:

- **Solid black arrows** represent the main forward path: stimulus → activity field → modal decomposition → amplitude dynamics → memory access → overlap → resonance → emission.

- **Dashed gray arrows** indicate additional relations within the model:
    - 3→2 (dashed): the modes are derived from the activity field via decomposition.
    - 6→5 (dashed): the overlap feeds back to the memory operator (learning / retrieval).
    - 7→2 (dashed): the amplified mode influences the original activity field, closing the recurrent loop.

The diagram is conceptual and intended to aid understanding of the mathematical formalism; detailed equations and their derivations are provided in Section 4.3 of the main text and in the Supplementary derivations.

S1.1. From light field to neural activity

The optical image projected onto the retina is described by a spatiotemporal brightness function $I(\mathbf{x}, \lambda, t)$. After spectral integration we obtain the luminance distribution $s(\mathbf{x}, t)$. The output of the early visual system is modeled as a continuous activity field $a(\mathbf{r}, t)$ (e.g., local field potential or spike density) in the visual cortex:

$$a(\mathbf{r}, t) = \int K_{\text{ret}}(\mathbf{r}, \mathbf{x})\, s(\mathbf{x}, t)\, d\mathbf{x} + \text{nonlinear terms.} \qquad \text{(S1)}$$

The kernel K_{ret} embodies retino-cortical mapping and receptive field properties.

S1.2. Modal decomposition

The activity field is expanded into a complete orthonormal set of spatial modes $\Phi_n(\mathbf{r})$:

$$a(\mathbf{r}, t) = \sum_n c_n\,(t)\Phi_n(\mathbf{r}), \qquad \text{(S2)}$$

where $c_n(t)$ are complex amplitudes (real parts correspond to physical quantities). The modes Φ_n represent stable excitation patterns such as cortical columns or resonant modes of CSF spaces.

S1.3. Dynamics of mode amplitudes

The amplitudes evolve according to:

$$\frac{dc_n}{dt} = \left(i\omega_n - \frac{1}{\tau_n}\right) c_n + \sum_m \Omega_{nm}\, c_m + f_n(t), \qquad \text{(S3)}$$

where ω_n are eigenfrequencies, τ_n damping constants, Ω_{nm} the synaptic interaction matrix, and $f_n(t)$ the projection of sensory input onto mode n.

S1.4. Long-term memory as an integral operator

Long-term synaptic changes are represented by an operator $\widehat{W}$ with kernel:

$$K(\mathbf{r}, \mathbf{r}') = \sum_n \lambda_n\, \Psi_n(\mathbf{r})\Psi_n(\mathbf{r}'), \qquad \text{(S4)}$$

where Ψ_n are eigenmodes of memory (engrams) and λ_n their weights. The overlap between the current state and an engram is:

$$\mu_k(t) = \langle a(\cdot, t), \Psi_k \rangle = \sum_n c_n\,(t)\langle \Phi_n, \Psi_k \rangle. \qquad \text{(S5)}$$

S1.5. Resonance and memory retrieval

When spatial resonance (| μ_k | maximal) and frequency resonance (| $\Omega(t) - \omega_k$ |< $\Delta\omega$) occur, the amplitude grows:

$$\frac{dc_k}{dt} = \left(i\omega_k - \frac{1}{\tau_k}\right) c_k + \gamma\, \sigma(|\, \mu_k \,|) c_k + f_k(t). \qquad \text{(S6)}$$

The sigmoid σ models threshold-dependent amplification.

S1.6. Microwave generation

Coherent oscillations generate alternating currents $\mathbf{J}(\mathbf{r}, t) = \sum_n \dot{c}_n\,(t)\mathbf{p}_n(\mathbf{r})$, and the recorded microwave power at frequency ω is:

$$P(\omega, t) \propto | \sum_{n:|\omega_n - \omega|<\delta} \dot{c}_n\,(t)\, |^2. \qquad \text{(S7)}$$

Thus spectral peaks correspond to active modes; the number of “substantial spikes” is proportional to the number of such modes.

S2. Complete Derivation of the Information-Based Model

While the energy-based model explains **how** microwave emission arises, we introduce an information-based model to address **why** spectral patterns change with cognitive state. This model shifts focus from energy to structural information.

S2.1. Supplementary Figure S2. Schematic representation of the information-based model of cognitive processing. The diagram illustrates the flow of information from the visual stimulus to the recorded microwave emission, integrating sensory processing, working memory, long-term memory and resonant retrieval.

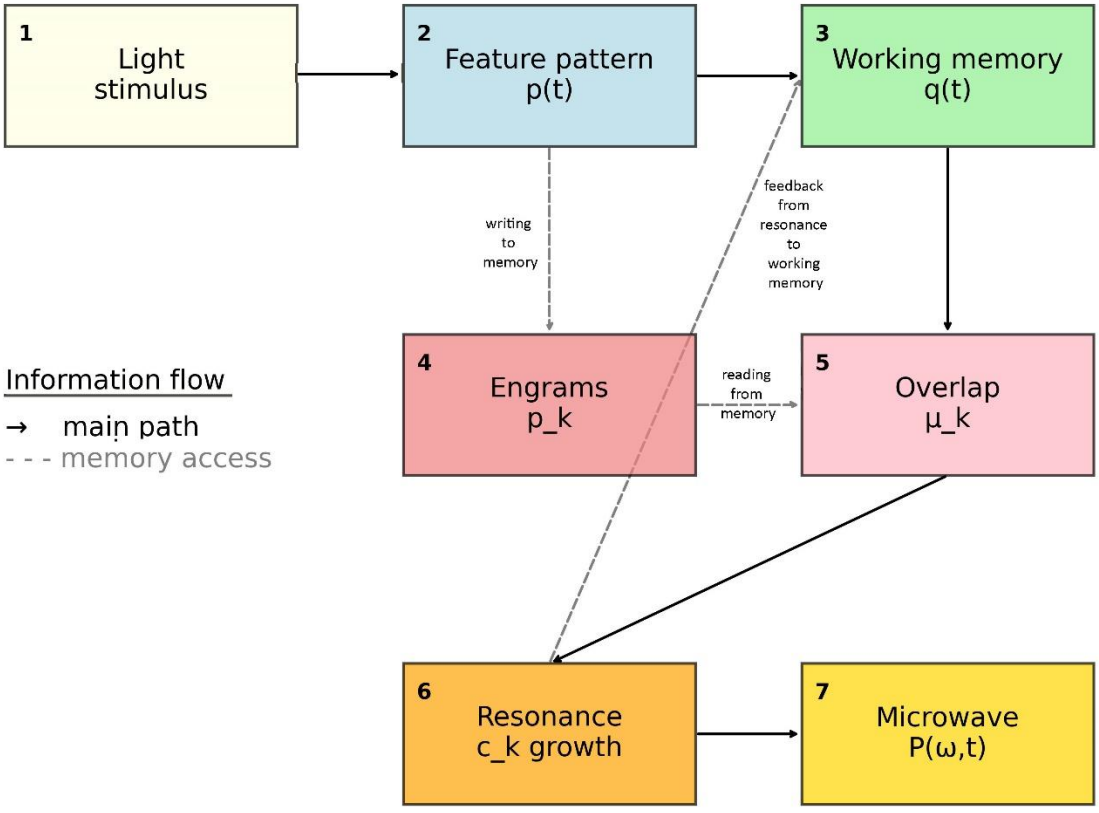

Fig. S2. Schematic representation of the information-based model of cognitive processing.

The diagram illustrates the flow of physical quantities from the visual stimulus to the recorded microwave emission, presented in Section 4.3 of the main text.

- **Block 1 (Light stimulus):** External visual input (light on/off) that initiates the process.
- **Block 2 (Activity field a(r,t)):** Continuous neural activity field representing local field potentials or spike densities in the visual cortex.
- **Block 3 (Modes $\Phi_n(r)$):** Spatial eigenmodes obtained by decomposing the activity field; each mode corresponds to a stable excitation pattern (e.g., cortical columns, CSF resonances).
- **Block 4 (Amplitudes $c_n(t)$):** Complex amplitudes that quantify the contribution of each mode to the total activity; their dynamics are governed by Eq. (2).
- **Block 5 (Memory operator K(r,r')):** Integral operator representing long-term synaptic changes; its kernel is expanded over engrams Ψ_n with weights λ_n (Eq. (3)).
- **Block 6 (Overlap μ_k):** Projection of the current field onto the k-th engram (Eq. (4)); it measures how close the current pattern is to a stored memory.
- **Block 7 (Resonance c_k growth):** When spatial and frequency resonance conditions are satisfied, the corresponding amplitude grows nonlinearly (Eq. (5)), corresponding to memory retrieval.
- **Block 8 (Microwave P(ω,t)):** The emitted microwave power, proportional to the squared sum of the time derivatives of the amplitudes (Eq. (6)), serving as the observable signal.

Arrows:

- **Solid black arrows** represent the main forward path: stimulus → activity field → modal decomposition → amplitude dynamics → memory access → overlap → resonance → emission.
- **Dashed gray arrows** indicate additional relations within the model:
  - 3→2 (dashed): the modes are derived from the activity field via decomposition.
  - 6→5 (dashed): the overlap feeds back to the memory operator (learning / retrieval).
  - 7→2 (dashed): the amplified mode influences the original activity field, closing the recurrent loop.

S2.2. Feature space and informational patterns

Let $\mathcal{P}$ be a space of informational patterns (features). The retinal output is transformed into an informational pattern $\mathbf{p}(t) \in \mathcal{P}$ via a nonlinear operator $\mathcal{F}$:

$$\mathbf{p}(t) = \mathcal{F}[s(\mathbf{x}, t)]. \qquad \text{(S8)}$$

S2.3. Working memory dynamics

Working memory $\mathbf{q}(t) \in \mathcal{P}$ evolves as:

$$\frac{d\mathbf{q}}{dt} = -\frac{1}{\tau}\mathbf{q} + \alpha\mathbf{p}(t) + \beta\widehat{M}[\mathbf{q}], \qquad \text{(S9)}$$

where τ is the decay time, α the input gain, and $\widehat{M}$ a recurrent operator (auto-associative recall).

S2.4. Long-term memory as a holographic operator

Long-term memory is represented by an operator $\widehat{K}$ with kernel expanded over stored engrams $\mathbf{p}_k$:

$$K(\mathbf{r}, \mathbf{r}') = \sum_k \lambda_k \, \mathbf{p}_k(\mathbf{r})\mathbf{p}_k(\mathbf{r}'). \qquad \text{(S10)}$$

The informational overlap is $\mu_k(t) = \langle \mathbf{q}(t), \mathbf{p}_k \rangle_{\mathcal{P}}$.

S2.5. Retrieval dynamics

Expanding $\mathbf{q}(t) = \sum_k c_k(t)\mathbf{p}_k$, the coefficients evolve as:

$$\frac{dc_k}{dt} = -\frac{1}{\tau}c_k + \alpha\langle \mathbf{p}, \mathbf{p}_k \rangle + \gamma\, \sigma(|\, \mu_k \,|)c_k. \qquad \text{(S11)}$$

When overlap exceeds threshold, the component grows, representing memory retrieval. The observed microwave power becomes an epiphenomenon:

$$P(\omega, t) \propto \sum_k |\, \dot{c}_k(t) \,|^2\, \delta(\omega - \omega_k). \qquad \text{(S12)}$$

S3. Additional Experimental Data

S3.1. Individual subject data from the 2025 experiment

Table S1. Spike counts for each subject in the 2025 experiment (mean ± SD over 8 repetitions)

Subject	Hemisphere	Light (mean ± SD)	Darkness (mean ± SD)	Difference (D-L)	p (paired t-test)
S1	Right	84.3 ± 4.2	86.1 ± 5.1	+1.8	0.12
S1	Left	91.2 ± 3.8	82.5 ± 4.6	–8.7	0.003
S2	Right	81.5 ± 5.0	83.8 ± 4.8	+2.3	0.08
S2	Left	88.9 ± 4.5	80.1 ± 5.2	–8.8	0.004
S3	Right	82.9 ± 4.7	83.3 ± 5.3	+0.4	0.76
S3	Left	88.4 ± 4.1	81.6 ± 4.9	–6.8	0.02

S3.2. Frequency distribution of spikes (2021 experiment)

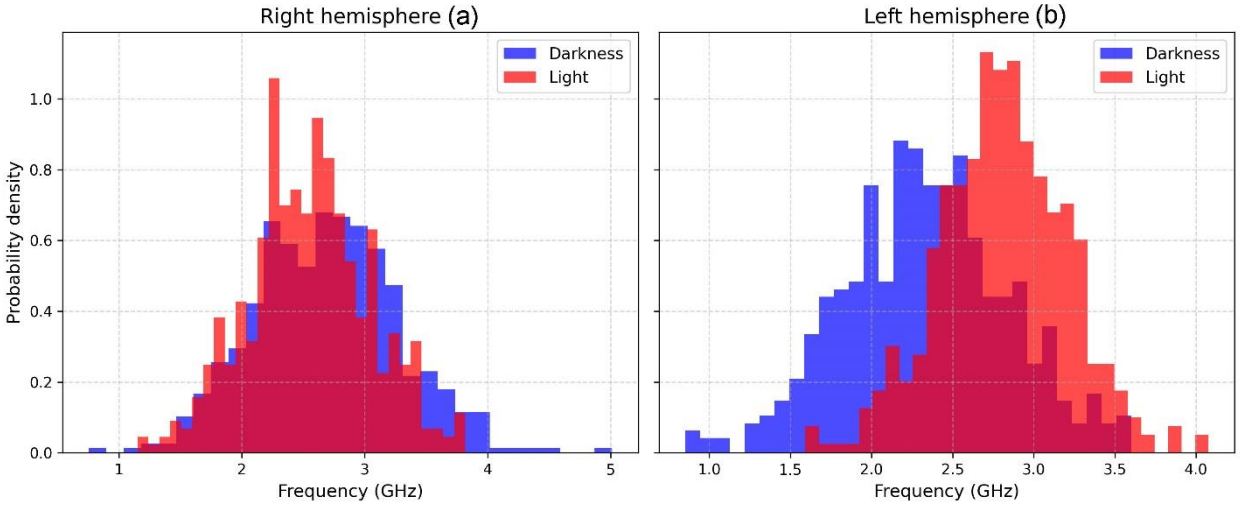

Fig. S3. Frequency distribution of microwave spikes in the 2021 experiment: (a) right hemisphere; (b) left hemisphere. Red – light, blue – darkness. Data pooled from all 150 measurements. For the right hemisphere, the distribution shifts toward higher frequencies in darkness; for the left hemisphere, the opposite is observed.

S3.3. Reproducibility across sessions (2021 experiment)

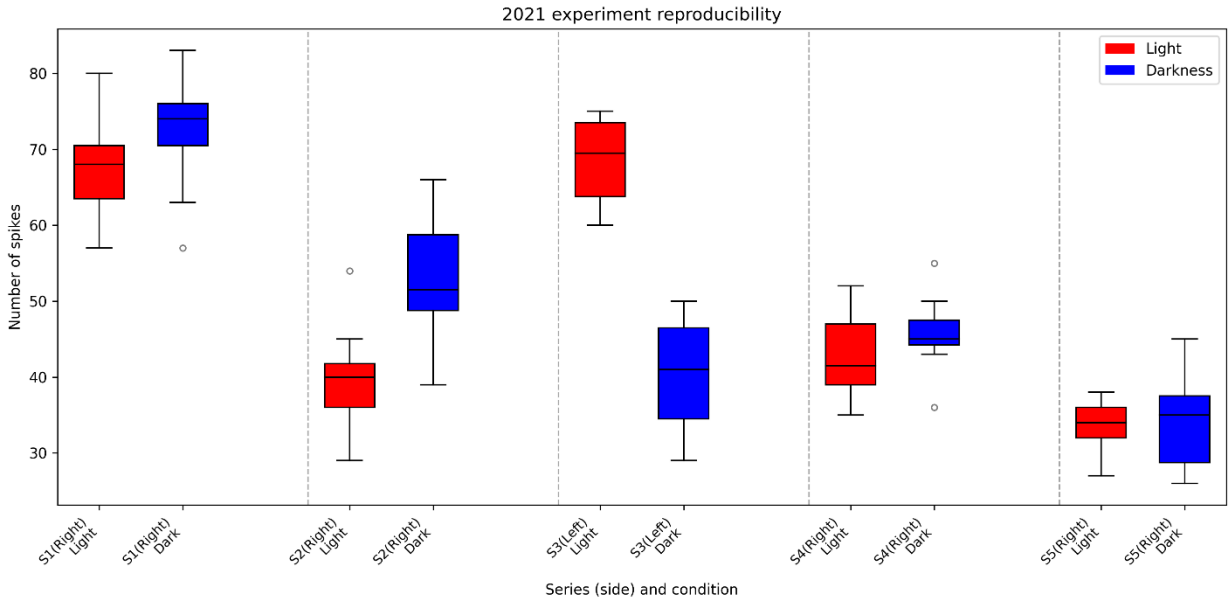

Fig. S4. Spike counts across sessions in the 2021 experiment. Each point represents one measurement; circles – light, squares – darkness. The difference between conditions is consistent across all series, confirming reproducibility.

S4. Extended Methodological Details

S4.1. Calibration and threshold selection

The spike detection threshold was set empirically based on the noise distribution in empty-chamber recordings: 2.2 dB corresponds approximately to twice the standard deviation of the noise power, ensuring <5% false positives. For the 2025 experiment, a higher threshold (22 dB) was used due to different antenna gain; after calibration, the effective sensitivity was comparable.

S4.2. Software implementation

The MWENC program (Python 3.9) reads CSV files, subtracts the averaged background, and identifies peaks using scipy.signal.find_peaks with parameters: height = threshold, distance = 10 points, prominence = 1.5 dB. SSPIKES aggregates results and performs statistical tests using scipy.stats.ttest_rel.

S4.3. Data availability

Raw data and analysis scripts are available at Zenodo: https://doi.org/10.5281/zenodo.15739578.

End of Supplementary Materials